ADVANCED MATERIALS
www.advmat.de

Highly Efficient Wide Bandgap Perovskite Solar Cells With Tunneling Junction by Self-Assembled 2D Dielectric Layer

Minwoo Lee, Jihoo Lim, Eunyoung Choi, Arman Mahboubi Soufiani, Seungmin Lee, Fa-Jun Ma, Sean Lim, Jan Seidel, Dong Han Seo, Ji-Sang Park, Wonjong Lee, Jongchul Lim, Richard Francis Webster, Jincheol Kim, Danyang Wang, Martin A. Green, Dohyung Kim, Jun Hong Noh, Xiaojing Hao,* and Jae Sung Yun**

Reducing non-radiative recombination and addressing band alignment mismatches at interfaces remain major challenges in achieving high-performance wide-bandgap perovskite solar cells. This study proposes the self-organization of a thin two-dimensional (2D) perovskite BA_2PbBr_4 layer beneath a wide-bandgap three-dimensional (3D) perovskite $Cs_{0.17}FA_{0.83}Pb(I_{0.6}Br_{0.4})_3$, forming a 2D/3D bilayer structure on a tin oxide (SnO_2) layer. This process is driven by interactions between the oxygen vacancies on the SnO_2 surface and hydrogen atoms of the n-butylammonium cation, aiding the self-assembly of the BA_2PbBr_4 2D layer. The 2D perovskite acts as a tunneling layer between SnO_2 and the 3D perovskite, neutralizing the energy level mismatch and reducing non-radiative recombination. This results in high power conversion efficiencies of 21.54% and 19.16% for wide-bandgap perovskite solar cells with bandgaps of 1.7 and 1.8 eV, with open-circuit voltages over 1.3 V under 1-Sun illumination. Furthermore, an impressive efficiency of over 43% is achieved under indoor conditions, specifically under 200 lux white light-emitting diode light, yielding an output voltage exceeding 1 V. The device also demonstrates enhanced stability, lasting up to 1,200 hours.

1. Introduction

With the rapid development of the Internet of Things (IoT) and for a carbon-neutral society,[1] photovoltaics can play a crucial role in supplying a large amount of off-grid energy through efficient light-harvesting and conversion processes.[2] Perovskite solar cells (PSCs) are recognized as promising candidates for IoTs to operate as low-power consumption devices for indoor applications owing to their tunable bandgap and exceptional optoelectronic properties.[1c,3] The emission spectra of indoor light sources, such as light-emitting diodes (LEDs), are much narrower and have weaker intensity compared to that under standard 1-Sun illumination conditions (i.e., AM 1.5G)[4] shown in Figure S1 (Supporting Information). For this reason, the Shockley–Queisser limit shows the highest power conversion efficiency of indoor lights

M. Lee, J. Seidel, R. F. Webster, D. Wang
School of Materials Science and Engineering
University of New South Wales
Sydney, NSW 2052, Australia

M. Lee, J. Lim, E. Choi, F.-J. Ma, M. A. Green, X. Hao, J. S. Yun
Australian Centre for Advanced Photovoltaics (ACAP)
School of Photovoltaic and Renewable Energy Engineering
University of New South Wales
Sydney, NSW 2052, Australia
E-mail: xj.hao@unsw.edu.au; j.yun@surrey.ac.uk

A. M. Soufiani
Helmholtz-Zentrum Berlin für Materialien und Energie GmbH
Division Solar Energy
12489 Berlin, Germany

The ORCID identification number(s) for the author(s) of this article can be found under https://doi.org/10.1002/adma.202402053

DOI: 10.1002/adma.202402053

S. Lee, J. H. Noh
School of Civil, Environmental and Architectural Engineering
Korea University
Seoul 02841, Republic of Korea
E-mail: junhnoh@korea.ac.kr

S. Lim, R. F. Webster
Electron Microscope Unit
University of New South Wales
Sydney, NSW 2052, Australia

D. H. Seo
Energy Materials & Devices
Korea Institute of Energy Technology (KENTECH)
Jeollanam-do, Naju 58330, Republic of Korea

J.-S. Park
SKKU Advanced Institute of Nanotechnology (SAINT) and Department of Nano Engineering
Sungkyunkwan University
Suwon 16419, Republic of Korea

W. Lee, J. Lim
Department of Energy Science and Technology
Chungnam National University
Daejeon 34134, Republic of Korea

at between 1.8 and 1.9 eV which can achieve theoretical efficiency of up to 60%.[5]

To achieve high photovoltaic performance under indoor lighting conditions, certain characteristics are essential for solar cells. First, they should exhibit a photoresponse spectrum that aligns with the emission spectrum of indoor light sources, i.e., a bandgap between 1.8 and 1.9 eV. Second, effective suppression of trap-mediated charge recombination is crucial since the low incident light intensity in indoor environments corresponds to a low excess carrier density, making trap-mediated recombination more significant. Finally, it is important to minimize energy losses ($E_{loss} = E_g - qV_{OC}$, where E_g is the bandgap, q is the elementary charge, and V_{OC} is the open circuit voltage) to maximize the V_{OC}. A major factor contributing to the V_{OC} losses in wide bandgap PSCs is the energy band alignment mismatch.[6] Such losses could arise due to undesired interfacial band bending and reduced quasi-Fermi level splitting between the interfaces.[7] One potential approach to mitigate this band alignment mismatch is the implementation of charge-carrier tunneling layers. This strategy has been successful in silicon solar cells, where a tunneling layer is applied between the lightly-doped silicon substrate and a heavily-doped polysilicon or indium tin oxide (ITO) layer, utilizing a thin insulating layer such as silicon dioxide.[8] The insulating layer effectively passivates the silicon substrate and facilitates carrier transport, leading to the efficient separation of photogenerated electrons and holes.[9]

In our experimental study, we elucidate the role of a tunneling layer within two-dimensional (2D) perovskite films, specifically BA_2PbBr_4, which exhibits dielectric properties with a dielectric constant of 2,[10] in the development of high-performance wide-bandgap PSCs. Through a systematic exploration of alternative cations and halides, it was observed that pre-deposited n-BABr effectively facilitates the formation of a self-assembled 2D perovskite layer during the formation of a three-dimensional (3D) perovskite layer. This self-assembly process results in improved perovskite crystallinity and effectively ameliorates the band alignment discrepancies between the electron transport layer (e.g., tin oxide (SnO_2)) and the 3D perovskite layers. Consequently, this phenomenon results in the suppression of non-radiative recombination and an improved interfacial charge extraction process, demonstrating a high power conversion efficiency (PCE) of 19.16% for PSCs with a bandgap of 1.8 eV and 21.54% for PSCs with a bandgap of 1.7 eV (independently certified at 20.62%) under standard 1-Sun illumination conditions. Moreover, our fabricated devices exhibit exceptional performance characteristics, achieving an efficiency of 43.7% when tested under 200 lux white LED illumination in indoor conditions. Furthermore, the encapsulated devices demonstrate remarkable long-term stability, retaining their performance levels even after exposure to 1000 lux illumination in a nitrogen (N_2) atmosphere for a duration exceeding 1200 h.

2. Results and Discussion

The wide bandgap perovskite was fabricated with MA free (MA denotes methylammonium) and 40% concentration of bromide composition ($Cs_{0.17}FA_{0.83}Pb(I_{0.6}Br_{0.4})_3$) as named 3D perovskite. To form BA_2PbBr_4 which is also named a 2D perovskite layer at the interface of SnO_2 and 3D perovskite layers, we devised a strategy involving the use of n-Butylammonium Bromide (n-BABr) as seed as shown (Figure S2, Supporting Information). Hereafter, the 3D perovskite films and the corresponding devices synthesized by incorporating 2D perovskite under the 3D perovskite layer are referred to as the 'target' materials. Notwithstanding the solubility of n-BABr in polar solvents such as Dimethylformamide (DMF) and Dimethylsulfoxide (DMSO), the n-BABr layer endured even subsequent to the DMF solvent treatment, a fact corroborated by the contact angle measurements depicted in **Figure** 1a–d which show the contact angle before (30.12°) and after (31.95°) did not change after treated by DMF which leads to the proof of the n-BABr is exist after treated by DMF. To further investigate the underlying mechanism, we simulated hybrid density functional theory (DFT) calculations (see Figure 1e). The detailed DFT calculation results can be found in Figure S3 (Supporting Information). This phenomenon can be attributed to the robust interactions between hydrogen (H) of n-BABr and oxygen vacancy (V_O) of SnO_2, resulting in a strong bonding that hinders the removal of n-BABr. This observation is further supported by the analysis of X-ray photoelectron spectroscopy spectra (Figure S4, Supporting Information). Such interactions play a crucial role in preventing n-BABr from dissolving with the 3D perovskite precursor during the post-annealing process of the 3D perovskite film, thus promoting the self-assembly of 2D perovskites.

Through a detailed investigation of the robust interactions between V_O and SnO_2, we have successfully demonstrated the formation of a self-assembled layer of n = 1 2D perovskite BA_2PbBr_4 beneath the 3D perovskite layer, as depicted in Figure 1f. To verify this, we conducted High-Resolution Transmission Electron Microscopy (HR-TEM) for the formation of the BA_2PbBr_4. Figure 1g shows the cross-sectional HR-TEM image of an exemplary perovskite device with the formation of a 2D perovskite layer between SnO_2 and the 3D perovskite layers. There are two

J. Kim
New & Renewable Research Center Korea
Electronics Technology Institute
Seong-Nam 13509, Republic of Korea
J. Kim
School of Engineering
Macquarie University Sustainable Energy Research Centre
Macquarie University
Sydney, NSW 2109, Australia
D. Kim
Department of Advanced Materials Engineering
Chungbuk National University
Cheongju 28644, South Korea
J. H. Noh
KU-KIST Green School Graduate School of Energy and Environment
Korea University
Seoul 02841, Republic of Korea
J. H. Noh
Department of Integrative Energy Engineering
Korea University
Seoul 02841, Republic of Korea
J. S. Yun
School of Computer Science and Electronic Engineering
Advanced Technology Institute (ATI)
University of Surrey
Guildford, Surrey GU2 7XH, UK

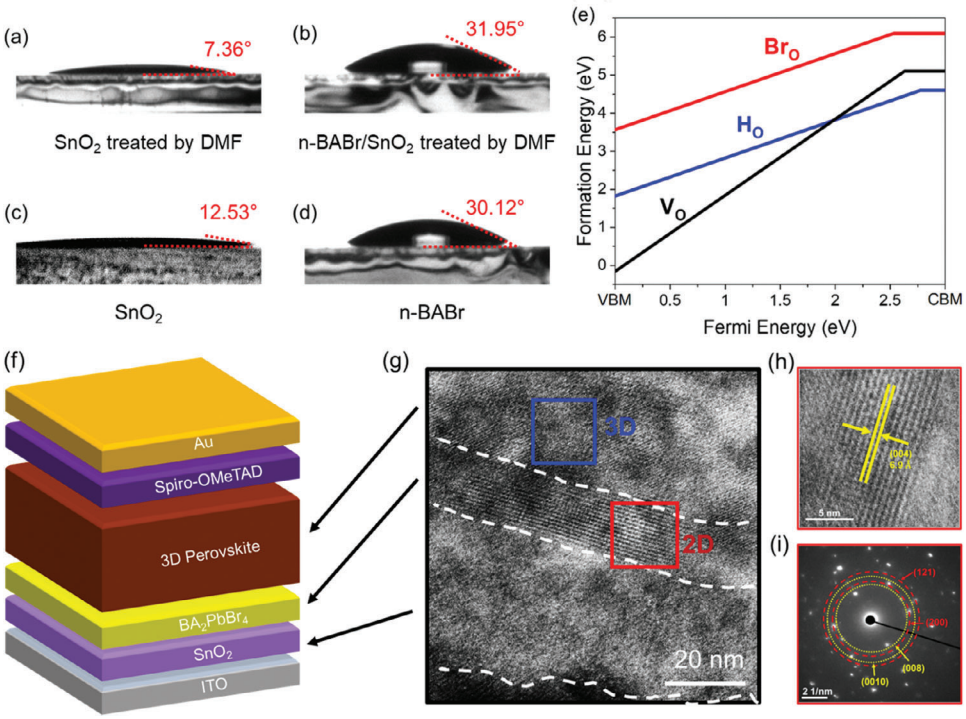

Figure 1. a–d) Contact angle of treated by DMF on (SnO_2, and -BABr/SnO_2), untreated by DMF (SnO_2, and n-BABr). e) DFT simulation results in hydrogen bonding with oxygen vacancies (H_O), bromide bonding with oxygen vacancies (Br_O) atoms, and oxygen vacancies (V_O). f) Device structure with the formation of BA_2PbBr_4 under 3D perovskite film. g) HR-TEM cross-sectional image of target perovskite devices. h) Lattice spacings of the 2D perovskite and i) SAED pattern for the bottom part of the 3D perovskite layer.

distinguished regions, 3D and 2D perovskites, marked by a blue and a red square, respectively. Figure 1h represents the 2D perovskite region which exhibits lattice spacing of 6.9 Å. We then compared the lattice spacing of 6.9 Å with the X-ray Diffraction (XRD results of standalone n = 1 BA_2PbBr_4 2D perovskite, which was fabricated stoichiometrically (see Figure S5, Supporting Information). The same lattice spacing was observed for the (004) planes, as presented in Table S1 (Supporting Information). Figure 1i shows the corresponding selected area electron diffraction patterns for the location. The bottom side of the perovskite layer exhibits the presence of both 3D and 2D perovskite patterns. This shows the existence of the self-assembled BA_2PbBr_4 2D perovskite formed through the reaction between existing n-BABr and 3D perovskite at the interface between SnO_2 and the 3D perovskite layer. The above results indicate the existence of a layer of 2D perovskite, BA_2PbBr_4 (n = 1), on SnO_2, with its (00n) planes parallel with the SnO_2 interface. We further selected and characterized other locations, the middle and upper part of the 3D perovskite far from the SnO_2/3D perovskite interface, (see Figure S6, Supporting Information). The only presence of a 2D perovskite layer beneath the 3D perovskite layer has been confirmed. Subsequently, we conducted experiments to investigate the properties of a 3D perovskite layer on the 2D perovskite layer.

In contrast to the control perovskite film, the target film displayed a notably improved morphology, characterized by significantly larger grain domains, as illustrated in Figure S7 (Supporting Information) through Scanning electron microscopy (SEM) analysis. This finding strongly implies that the self-assembly of BA_2PbBr_4 has yielded enhancements in the crystalline structure of the 3D perovskite film. Further investigations revealed that different types of organic salt seed layers significantly affect the crystallinity of the 3D perovskite layer. This is demonstrated by comparing two different types of A and X site organic salts (PEAI, PEABr, n-BAI, and n-BABr). Figure S8 (Supporting Information) shows the XRD patterns of the 3D perovskite layers with different organic salts as a seed layer. The n-BABr exhibits the highest crystallinity of the (100) perovskite plane, with an FWHM of 0.146, compared to PEAI (0.150), PEABr (0.152), and n-BAI (0.163). To investigate why such crystallinity difference occurs in the 3D perovskite layer, we performed a study on the interaction of various organic salts with the SnO_2 surface using X-ray Photoelectron Spectroscopy (XPS) after treatment of the organic salts with DMF, aiming to ascertain the presence and potential role of these salts in the formation of a 3D perovskite layer. Figure S9 (Supporting Information) illustrates distinct halide peaks (iodine at ≈619.64 eV, bromide at ≈68.94 eV) before and after DMF treatment. The iodine peak is absent after DMF treatment for PEAI (Figure S9a, Supporting Information). Conversely, n-BAI and PEABr show ≈50% reduction in iodine and bromine content post-DMF treatment, as depicted in Figure S9b,c (Supporting Information). Interestingly, the bromine XPS peak remains unaffected after DMF treatment of the n-BABr layer. This observation could be attributed to bromine's higher electronegativity (2.96) than iodine (electronegativity 2.66), facilitating stronger and more stable bonding with SnO_2. Additionally, contact angle measurements (Figure S10, Supporting Information) were conducted using different organic salts, revealing that the n-BA cation samples exhibit contact angles of 40.34° for n-BAI and

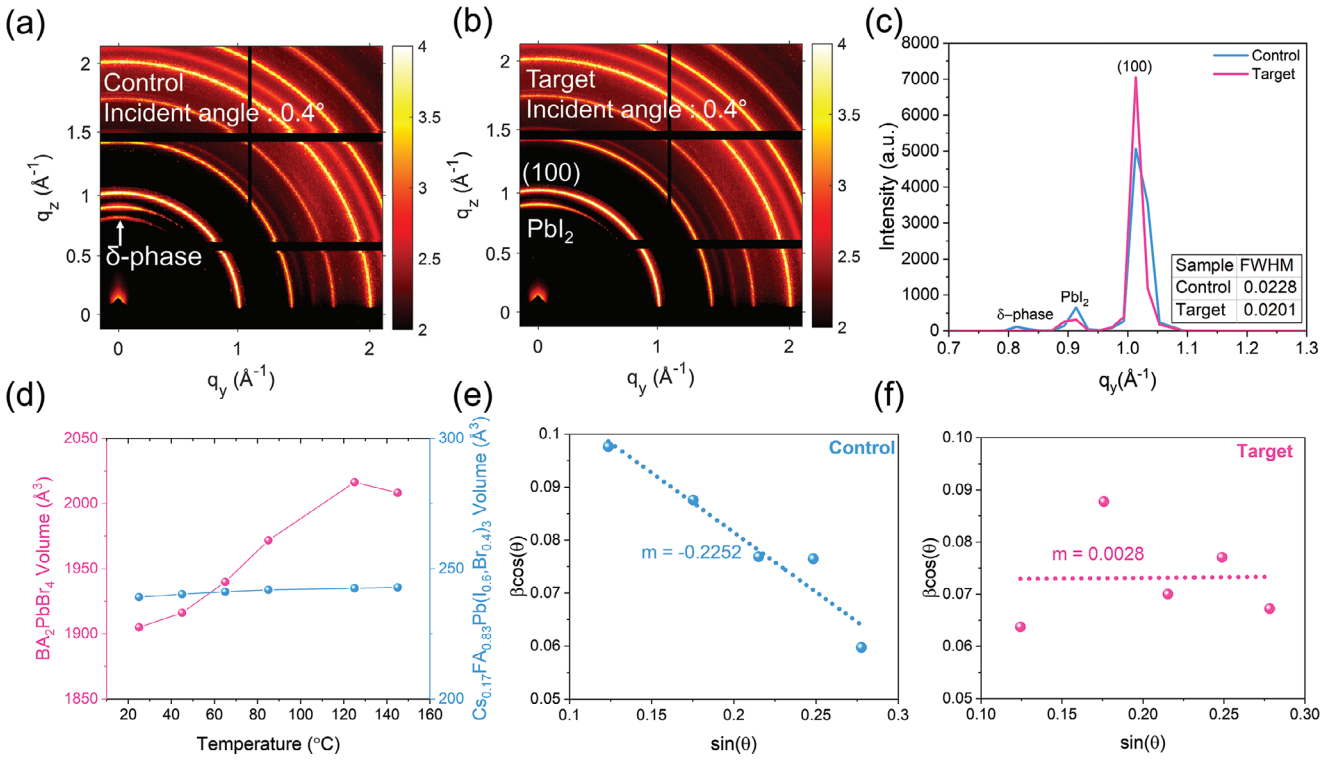

Figure 2. GIWAXS measurement with 0.4° incident angle measurements of a) the control and b) the n-BABr perovskite films. c) Intensity plots of the (100) crystal plane, obtained from 2D GIWAXS patterns in the control and the n-BABr perovskite films. d) Thermal expansion coefficient measurement of BA_2PbBr_4 and 3D perovskite film. XRD Williamson–Hall plot of e) the control sample and f) the sample with underlying pre-deposited n-BABr.

38.01° for n-BABr, while the PEA cation samples show contact angles of 42.45° for PEAI and 56.71° for PEABr. These results indicate that the n-BA cation has better hydrophobicity compared to the PEA cation. This can be attributed to the polar C—H bonds in the n-BA butyl group, which enhance interactions with polar groups on the SnO_2 surface. Therefore, the stronger interaction of n-BABr with the SnO_2 layer explains why bromine fully remained after DMF treatment, whereas iodine from PEAI is completely removed. These results are summarized in Table S2 (Supporting Information). As a result, the remaining layer of n-BABr which has the stronger interaction with the SnO_2 surface has the most significant impact, thereby assisting the growth of the 2D BA_2PbBr_4 layer and the improves the crystallinity of the 3D perovskite layer, as evident from the SEM images in Figure S11 (Supporting Information). The images reveal that PEAI, PEABr, and n-BAI result in inhomogeneous grains (highlighted in red circles), which may indicate a secondary phase such as PbI_2.[11]

2D grazing-incidence wide-angle X-ray scattering (GIWAXS) was employed to analyze the bulk microcrystalline structure of the control and target perovskite films at an incident angle of 0.4°, as illustrated in **Figure 2**a,b. All samples are dominated by crystallites with the (100) plane oriented in the out-of-plane direction, as shown in Figure 2c. This represents the direction of the film surface perpendicular to the substrate, which corresponds to Q_z in 2D GIWAXS. The control perovskite film shows the δ-phase at 0.81 Å^{-1} and the PbI_2 at ≈0.91 Å^{-1}, indicating that the pure α-phase of the (100) perovskite structure has not completely formed, while the target film does not show the δ-phase and the less PbI_2. Moreover, there is a stronger σ-phase of (100) perovskite at ≈1.01 Å^{-1} for the target film (See the GIWAXS profile in Figure 2c with higher crystallinity as evidenced by a smaller FWHM. Figure S12 (Supporting Information) also indicates the GIWAXS profile of the (200) plane which is consistent with the (100) plane.

In the following, we discuss a potential factor that has resulted in an improved crystallinity of the target sample. We hypothesize that the underlying BA_2PbBr_4 2D perovskite can act as a buffer layer minimizing the thermal expansion coefficient (TEC) difference between the 3D perovskite and SnO_2 layers. As shown in Figure 2d, we performed temperature-dependent XRD measurements on a thick BA_2PbBr_4 2D (≈300 nm thick) and 3D perovskite layers from which TECs were obtained. Our calculation shows that the TEC for 2D and 3D perovskites are 5.18×10^{-4} and 1.24×10^{-4} °C^{-1}, respectively. The detailed calculation can be found in the Experimental Section. It has been reported that SnO_2 exhibits a TEC of 3.23×10^{-6} °C^{-1}.[12] The large difference in TEC between SnO_2 and the 3D perovskite can result in significant strain and stress at their interface. The 2D perovskite's TEC, while still higher than SnO_2, is closer to the TEC of the 3D perovskite than SnO_2 which means that the 2D perovskite layer can act as a buffer, absorbing some of the differential expansion and contraction between the SnO_2 and 3D perovskite layers. This approach can potentially enhance the structural stability and overall performance of the perovskite solar cells.[13] In the following, we performed the Williamson–Hall analysis of the XRD spectra, which provides information about strain in the perovskite

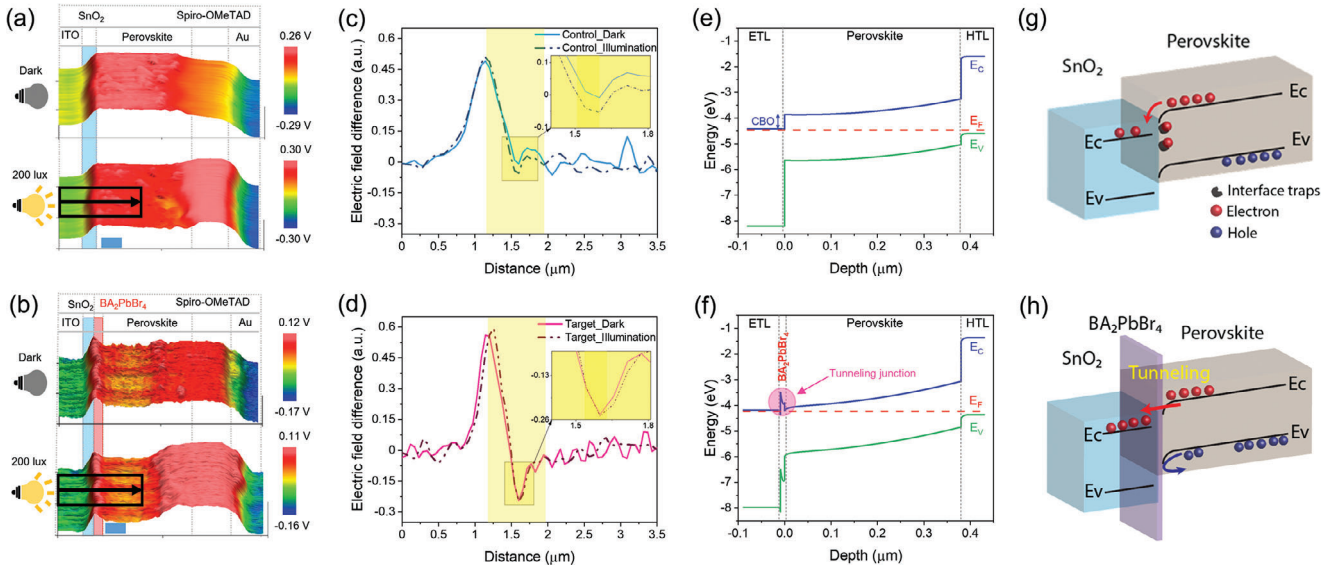

Figure 3. Cross-sectional KPFM and schematic illustration for the tunneling effect of BA_2PbBr_4. a) CPD image of the control device and b) CPD image of the target device under dark and illumination conditions. The scale bar corresponds to 1 μm. Electric field difference of c) the control device and d) the target device, extracted from a selected region marked by the black rectangular box with the arrow in the image. Note that cross-sectional KPFM is measured in short-circuit conditions. TCAD simulation of the band diagram for e) the control device and f) the target device. Schematic illustration of the electron transportation with g) and without h) tunneling layer.

structure. Figure 2e shows that the control sample exhibits a compressive strain,[14] while Figure 2f shows that the strain is suppressed by the 2D perovskite on the SnO_2 layer. Next, a depth-dependent GIWAXS measurement (Figure S13, Supporting Information) was conducted to examine the crystallinity at the surface (0.1°) and bulk (0.4°) of the 3D perovskite layer.[15] Due to the presence of comprehensive strain, the peak position of the (100) plane in the control film is different between surface and bulk, while the target film shows constantly the same position regardless of the depth surface and bulk of perovskite film, indicative of the formation of uniformly reduced strain across the film thickness.[13a]

To elucidate the charge transport properties of the target sample, we conducted a cross-sectional Kelvin Probe Force Microscopy (KPFM). A schematic of the KPFM measurement under short-circuit conditions is shown in Figure S14 (Supporting Information) and further KPFM measurement details can be found in the Experimental Section. The corresponding topography images can be found in Figure S15a,b (Supporting Information), respectively. **Figure 3**a shows a cross-sectional KPFM image of the control sample. There is a small fluctuation across the SnO_2/perovskite interface. However, Figure 3b indicates that there is a noticeable increased contact potential difference (CPD) at the SnO_2/perovskite interface due to the existence of the BA_2PbBr_4 layer which has a different work function. As can be seen, the layer induces a higher potential valley at the interface that could be seen as a barrier to electron transport. Figure 3c,d illustrate the electric field difference between the SnO_2 and perovskite layers for the control and target samples, based on the CPD distribution shown in Figure 3a,b. Under illumination conditions for the control sample, as depicted in Figure 3c, there is a difference of (0.05) before and after the illumination for the electric field difference at the SnO2/perovskite interface as shown in the inset of Figure 3c. This implies that electrons are trapped or accumulated at the interface of the SnO_2/perovskite layer, as the samples were connected in a short circuit condition. In contrast, for the target sample, there is no such electric field difference after the illumination condition compared to that of the dark as shown in the inset of Figure 3d. This indicates that charges were not accumulated at the interface, facilitated by the BA_2PbBr_4 2D perovskite layer, which aids in the efficient transfer of charges from the perovskite to the SnO_2 layer. To further scrutinize the disparity in CPD, we have acquired line profiles spanning the interface, as depicted in Figure S16a,b (Supporting Information). There is a dramatic difference in the slope of the CPD profile, the target device exhibits a steeper slope of −0.244, compared to that of the control device, which is −0.041. Interestingly, under light illumination, this layer enables efficient transfer of the electrons from perovskite to the SnO_2 layers which was confirmed by the CPD line profiles in the dark and under illumination in Figure S16a,b (Supporting Information). There is a larger gap (≈47 mV) for CPD variation for the control device due to more trapped charges at the SnO_2/perovskite interface, resulting in V_{OC} loss.[16] However, such a gap is almost negligible (≈8 mV) for the target device which implies that the charge carrier has efficiently moved throughout the 2D perovskite layer which leads to suppressing the non-radiative recombination. In addition, CPD under illumination for the control device is lower than that of CPD measured in the dark, which is attributed to trapped electrons at the interface. On the contrary, CPD under illumination is higher than in dark for the target device, due to enhanced electron transportation induced by the existence of the 2D perovskite. The results unequivocally demonstrate that the 2D perovskite layer of BA_2PbBr_4 serves as an effective tunneling barrier, facilitating electron transport, even in the presence of a differing work function compared to the contact layers.

To further validate this effect, we conducted simulations using Sentaurus Technology Computer-aided Design (TCAD) to assess the influence of the tunneling layer on carrier extraction. Figure 3e,f shows the simulated band diagram by TCAD of the SnO_2/perovskite/Spiro-OMeTAD device as the control sample and the SnO_2/BA_2PbBr_4/perovskite/Spiro-OMeTAD device as the target sample. From Figure 3e, the control sample exhibits a cliff-like conduction band offset (CBO) from the perovskite layer to SnO_2. The CBO exceeds 0.5 eV, acting as a high energy barrier against electron injection at the forward bias condition. High recombination is expected as more electrons are trapped at the interface. The case of the target sample exhibits one spike-like CBO and one cliff-like CBO in the band diagram depicted in Figure 3f. The spike-like CBO between the perovskite and BA_2PbBr_4 is moderate, allowing sufficient electron transport. The cliff-like CBO between BA_2PbBr_4 and SnO_2 is higher than that in the control sample. However, it helps induce a strong upward bending within BA_2PbBr_4. Although the energy barrier is higher and very narrow, it facilitates electron tunneling which confirms the above cross-sectional KPFM results. We further conducted Space Charge-Limited Current (SCLC) measurements shown in Figure S17 (Supporting Information), which shows that the control samples have a higher trap density of 2.18×10^6 cm^{-3} than the lower trap density of 1.90×10^6 cm^{-3} of the target samples, likely due to better electron transport through the BA_2PbBr_4 layer. In addition, we conducted a simulation of the tunneling effect dependent on the different thicknesses of the BA_2PbBr_4 layer, controlled by the concentration of n-BABr, as shown in Figure S18 (Supporting Information). The empty symbols in Figure S18 (Supporting Information) display the *J*–*V* performance for varying thicknesses of the BA_2PbBr_4 layer. The improved *J*–*V* performance of the sample with a 9 nm thick tunneling layer, compared to the control sample, is evident. However, this performance decreases as the tunneling layer's thickness increases, indicating that an optimal thickness (9 nm) is necessary to achieve the tunneling effect of the 2D perovskite layer. The *J*–*V* performance with solid lines in Figure S18 (Supporting Information) indicates simulation data based on the circle spots to verify the effect of charge tunneling between the 3D perovskite and SnO_2. The pink solid line represents the *J*–*V* data with the BA_2PbBr_4 tunneling layer, and the purple solid line indicates the control sample derived from the actual *J*–*V* data of the circle spots. Based on the simulated information, if the BA_2PbBr_4 does not exhibit a tunneling effect, the simulated BA_2PbBr_4_no tunneling with a green solid line shows an S-shaped curve, attributed to increased series resistance and reduced open-circuit voltage. Thus, the optimal thickness of BA_2PbBr_4 plays a significant role in improving device performance.

Furthermore, Figure S19a,b (Supporting Information) shows that the target device exhibits a broader depletion region of 175 nm compared to the control device, which is 116 nm. This not only can improve charge separation, and collection of photogenerated carriers but also suppresses the reversal of electron transportation from SnO_2 to the perovskite layer as well as reduces series resistance.[17]

Subsequently, we performed steady-state photoluminescence (PL) measurements on both the control and target devices, employing a 510 nm laser for excitation. This investigation aimed to elucidate the charge transport dynamics within the ITO/SnO_2/(with or without BA_2PbBr_4)/perovskite structure (refer to Figure S20, Supporting Information). The results obtained from this analysis further supported our hypothesis by demonstrating a notable reduction in non-radiative recombination in the target samples.

The conducted experiments have substantiated the tunneling characteristics exhibited by the 2D perovskite layer under 1-Sun illumination conditions across a spectrum of photovoltaic devices with varying bandgaps. The diagram in Figure S21a (Supporting Information) displays the V_{OC} line profiles for different bandgaps (1.55, 1.7, and 1.8 eV) and their S-Q limit. A bandgap of 1.55 eV was found to have a small improvement with the BA_2PbBr_4 tunneling layer, while the wide bandgaps of 1.7 and 1.8 eV showed greater improvement in the tunneling effect, reaching V_{OC} of 1.3 and 1.33 V, respectively. Figure S21b (Supporting Information) also shows a decrease in V_{OC} deficits, with values of 0.38, 0.42, and 0.5 for 1.55, 1.7, and 1.8 eV bandgaps respectively. Table S3 (Supporting Information) indicates the best *J*–*V* parameters of control and target devices with different bandgap under 1-Sun illumination condition. This enhanced tunneling effect is particularly significant for wide bandgap perovskite solar cells. The *J*–*V* characteristics for the energy bandgaps of 1.7 and 1.8 eV, corresponding to PCE of 21.54% (certified 20.62% Figure S22, Supporting Information) and 19.16% for target samples, are illustrated in **Figure 4a** and Figure 4b, respectively. However, the control samples exhibit PCE of 19.24% for the 1.7 eV bandgap and 16.44% for the 1.8 eV bandgap, respectively. In Figure 4c, the stabilized power output data during the 20 min of operational time is presented. The graph demonstrates that the power output remains constant throughout the light soaking period, caused by effective charge transportation and a strain-free perovskite structure. In addition, we investigated the PL intensity dependence for both the control and target perovskite films to examine halide segregation further, as shown in Figure S23 (Supporting Information). It indicates that at higher PL intensities starting from 2.50 Sun, the control sample exhibits a shoulder at longer wavelengths, which suggests the presence of halide segregation. In contrast, the target sample shows no additional shoulder, even at 25.04 Sun, compared to the control sample. Consequently, the chronic issues related to halide segregation for wide bandgap perovskite are successfully suppressed with the 2D perovskite layer between SnO_2 and 3D perovskite layers. Figure 4d demonstrates the V_{OC} across different bandgaps, referencing prior literature. The V_{OC} deficit represents a significant limitation for wide bandgap to perform the perovskite solar cells. Nonetheless, the integration of a 2D perovskite layer has markedly mitigated this deficit compared, resulting in achieved higher device performance under 1-Sun conditions.

Since wide bandgap solar cells (optimum bandgap ≈1.9 eV) can take the most benefit in harvesting indoor light,[4] we tested our devices under indoor light conditions. Figure 4e displays the *J*–*V* characteristics of the champion devices, comparing both the control and the target perovskite films. These measurements were conducted under an illumination intensity of 200 lux, utilizing a white LED source. It is worth noting that this lower light intensity, falling within the range of 200–1000 lux, simulates indoor conditions commonly encountered in residential and office conditions.[4] The illumination spectrum can be found in Figure S24 (Supporting Information). The highest PCE of target

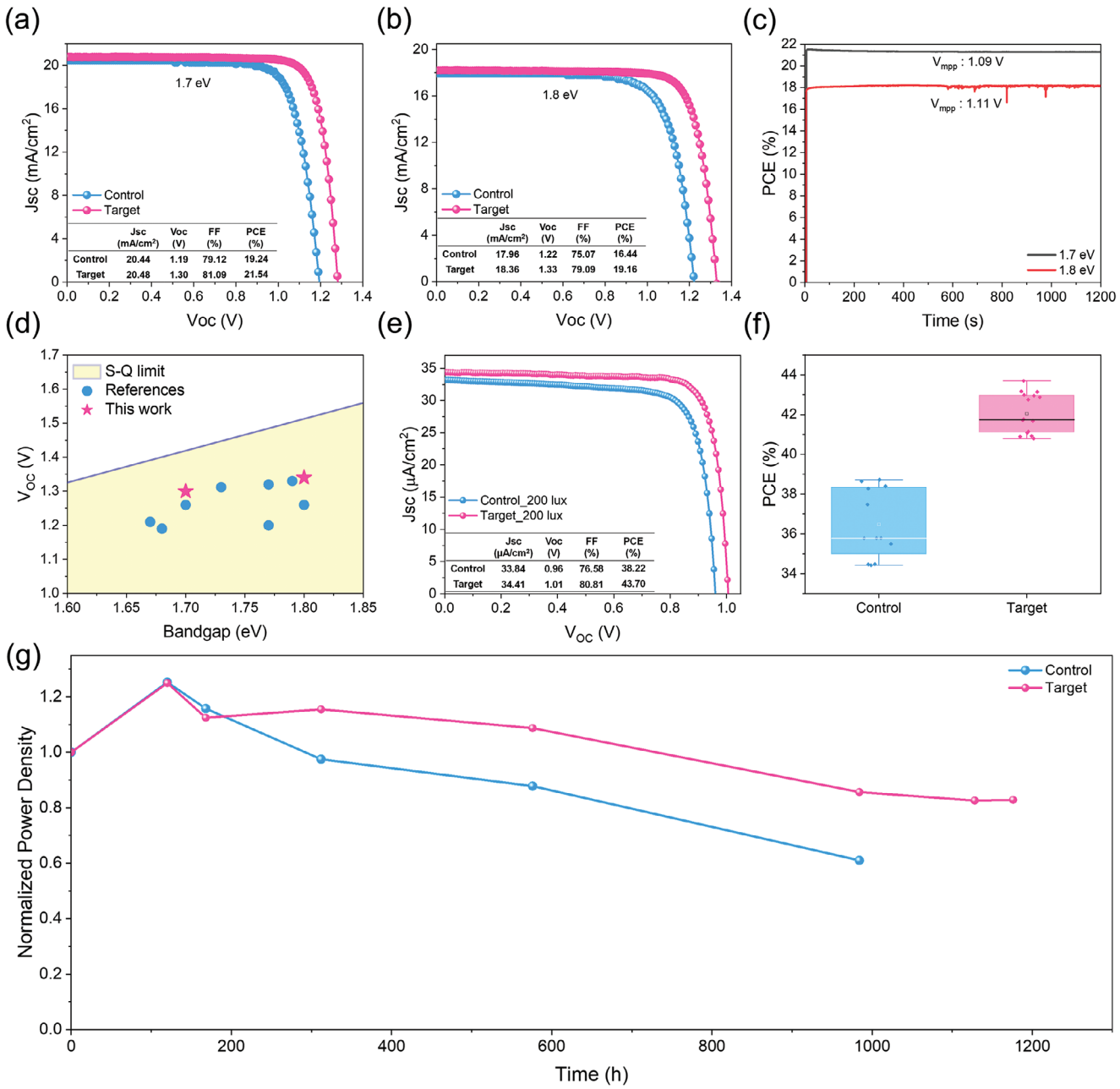

Figure 4. *J–V* curves (reverse scan) of the champion control and target samples with a) 1.7 eV and b) 1.8 eV bandgaps under 1-Sun conditions. c) Stabilized power output of both 1.7 eV (V_{mpp}: 1.09 V) and 1.8 eV (V_{mpp}: 1.11 V) wide bandgap perovskite devices. d) comparison of the V_{OC} of the wide bandgap PSCs in this work with the reported literature.[18] e) *J–V* curves (reverse scan) of the champion control and target-based devices measured under 200 lux light intensity using white LED illumination. f) Statistical distribution of PCE of the control and target perovskite devices g) Operational stability test results of encapsulated devices measured under 1000 lux light intensity and N_2 ambient using a white LED source.

devices was achieved at 43.70%, which is ≈14% higher than that of the control device, i.e., 38.22%. The lux intensity-dependent results of *J–V* measurement are shown in Table S4 (Supporting Information). The improvements have been also reflected in the internal quantum efficiency (IQE) of the two device structures, shown in Figure S25 (Supporting Information). It is likely that the enhanced IQE at a shorter wavelength range (<400 nm) is due to the reduced non-radiative recombination as well as carrier tunneling at the front interface, where the BA_2PbBr_4 layer is incorporated. The IQE improvement in the visible range might reflect the increased charge extraction efficiency of the target devices. From Figure 4f, the box plot of target devices measured under 200 lux white LED illumination exhibited a much higher average PCE of ≈42% compared to the control device of 36%. In addition, Figure S26 (Supporting Information) shows a much lower hysteresis index for the target device of 0.034 compared to the control device of 0.092, which is consistent with the enhanced electron extraction observation facilitated by the tunneling effect

of the BA_2PbBr_4 layer.[19] We then conducted a long-term operational stability test on the encapsulated devices under 1000 lux light intensity in N_2 ambient. After 1200 h of continuous illumination, as can be seen in Figure 4g, the target device and control device maintained ≈83% and ≈61% of their initial efficiency, respectively. As a result of the tunneling effect, the performance of the device and light soaking stability have been improved.

3. Conclusion

In summary, we have demonstrated a tunneling layer between SnO_2 and the perovskite layers using self-assembled 2D BA_2PbBr_4 for wide bandgap PSCs. This layer mitigated the carrier loss due to the mismatch of band alignment for wide bandgap PSCs. In addition, the enhanced crystal growth of the 3D perovskite layer and suppressed strain were performed. As a result, we demonstrated high V_{OC} of 1.3 and 1.33 V, resulting in an efficiency of 21.54% (1.7 eV) and 19.16% (1.8 e), respectively. Also, our device performance under low light intensity for indoor conditions is significantly enhanced to a PCE of 43% and remained at 83% of the initial PCE after 1200 h under 1000 lux of white LED illumination in the N_2 atmosphere.

4. Experimental Section

Materials: All materials were purchased from Sigma–Aldrich, TCI, Alfa Aesar, Dysol, Greatcell Solar and Lumtec.

Device Fabrication: Perovskite solar cell devices were fabricated with an Au/Sprio-OMeTAD/Perovskite/SnO_2/ITO structure. First, a glass substrate with indium tin oxide (ITO) was cleaned by sonication and rinsing in distilled water, acetone, and isopropanol. After drying using N_2, the substrate was treated using UV-Ozone for 15 min. For deposition of the SnO_2 electron transport layer (ETL), SnO_2 (15% in H_2O, colloidal dispersion from Alfar Aesar) was diluted by adding distilled water at a volume ratio of 1:5 (SnO_2: DI water). The diluted SnO_2 solution was dropped on the ITO glass and spin-coated at 3000 rpm for 30 s followed by annealing at 150 °C for 30 min.

The interlayers were processed by spin coating at 5000 rpm for 30 s with 100 µL of n-BABr dissolved in isopropanol on the SnO_2 layer and a subsequent annealing step at 100 °C for 5 min. The optimized $Cs_{0.17}FA_{0.83}Pb(I_{0.6}Br_{0.4})_3$ perovskite precursor solution was prepared by dissolving the mixture of CsI, FAI, PbI_2, and $PbBr_2$ in DMF: DMSO = 4:1 (v:v). The compact perovskite absorber layers were deposited on the substrates with a spin-coating procedure: first at 1000 rpm for 10 s and second at 5000 rpm for 30 s. For the anti-solvent, 200 µL of chlorobenzene was dropped on the spinning substrate during the second spin-coating step, 5 s before the end of the procedure. The film-coated substrate was then transferred onto a hotplate and annealed at 150 °C for 30 min. After cooling down, 2 mg of the n-BABr layer was deposited on the perovskite film at 4000 rpm for 20 s by spin coating. After that, the samples were moved to the hotplate at 100 °C for 5 min. The hole-transport layer (HTL) was subsequently deposited on top of the perovskite film by spin coating at 4000 rpm for 20 s using a chlorobenzene solution containing 90.9 mg Spiro-OMeTAD, 35.4 µL 4-tert-butylpyridine and 20.9 µL of lithium bis(trifluoromethanesulfonyl)imide solution (520 mg mL^{-1} in acetonitrile). Finally, An 80 nm Au contact layer was deposited on top of Spiro-OMeTAD using thermal evaporation. The active area of the electrode was at 0.25 cm^2.

Electron-only devices for SCLC were fabricated with a structure of Au/PCBM/Perovskite/SnO_2/ITO. The thickness of the perovskite of the hole-only devices was ≈360 nm. Spin-coating and evaporation procedures are identical to those mentioned above.

1.55 eV of Middle Bandgap Perovskite Film Fabrication: The $(FAPbI_3)_{0.98}(MAPbBr_3)_{0.02}$ perovskite precursor solution was prepared by mixing 0.2191 g of FAI, 0.5873 g of PbI_2, 0.0125 g of $MAPbBr_3$, 0.0272 g of MACl in 0.63 mL of DMF and 0.09 mL of DMSO mixed solvent. Then, the precursor solution was coated on the SnO_2 substrate using a one-step coating method, which consisted of 1000 and 5000 rpm for 5 and 15 s, respectively. Diethyl ether (1 mL) was poured on the spinning substrate at 13 s after starting at 5000 rpm. The yellow film was transferred to a hotplate at 150 °C and annealed for 20 min. Next, 12.5 mM octylammonium bromide in chloroform was coated at 5000 rpm for 30 s, and the coated film was heat-treated at 100 °C for 10 min.

1.7 eV of Wide Bandgap Perovskite Film Fabrication: The interlayers were processed by spin coating at 5000 rpm for 30 s with 100 µL of n-BABr dissolved in isopropanol on the SnO_2 layer and a subsequent annealing step at 100 °C for 5 min. The optimized $Cs_{0.17}FA_{0.83}Pb(I_{0.77}Br_{0.23})_3$ perovskite precursor solution was prepared by dissolving the mixture of CsI, FAI, PbI_2, and $PbBr_2$ in DMF: DMSO = 4:1 (v:v). The compact perovskite absorber layers were deposited on the substrates with a spin-coating procedure: first at 1000 rpm for 10 s and second at 5000 rpm for 30 s. For the anti-solvent, 200 µL of chlorobenzene was dropped on the spinning substrate during the second spin-coating step, 5 s before the end of the procedure.

2D BA_2PbBr_4 Perovskite Film Fabrication: The 2D perovskite precursor solutions were prepared by dissolving the mixture of $(n\text{-}BABr)_2$ and $PbBr_2$ in DMF:DMSO = 4:1 (v:v). The 2D perovskite layers were deposited on the ITO substrates with a spin-coating procedure at 5000 rpm for 25 s. For the antisolvent, 200 µL of CB was dropped on the spinning substrate at 20 s followed by annealing at 100 °C for 5 min.

Device Characterization: *J–V* characteristics of the devices were measured using a Keithley 2400 source meter under 100 mW cm^{-2} (AM 1.5G) illumination by a solar simulator (Sun 3000, Abet technologies). *J–V* characteristics of devices for indoor conditions were conducted under a cool white LED (PBA-0822-CW-04A, RFSemi) with 200 lux. Before measurement, the intensity of the LED lamp was calibrated using a digital lux meter. The working area was defined by a photomask with an aperture area of 0.25 cm^2.

External Quantum Efficiency (EQE) Measurement: Measured using EQE measurement system (QEX10, PV Measurements, Inc.) with 530 nm of the light source.

HR-TEM: The TEM Lamella sample for HR-TEM was prepared by the Focus Ion Beam (FIB) (FEI NoVa Nanolab 200) using the ex situ lift-out method. The cross-sectional TEM images were obtained by using a high-resolution TEM instrument (JEOL JEM-F200) with an acceleration voltage of 200 kV. To prevent damage to the perovskite sample the HR-TEM was used in a low dose with an exposure time of below 1 s for each image taken.[20]

SEM was utilized by FEI Nova NanoSem 230.

XPS was conducted by using (ESCALAB250Xi, Thermo Scientific) with an Al Kα X-ray source.

KPFM: For cross-sectional KPFM measurement, devices were milled to conduct a bevelled cross-section by a FIB using an FEI Nova nanolab 200 system with a 6° angle between the incident Ga+ ion beam and sample surfaces. Milling was performed in two steps sequential procedure: First (30 kV, 1 nA) and followed by (30 kV, 100 pA). Prepared devices mounted on a metal disc and the ITO layer of the device was grounded. KPFM was carried out in dark and illumination conditions by using a commercial AFM system (AIST-NT SmartSPM 1000) using a Ti/Ir-coated tip (ASYLELEC-02). The thickness of each layer could be expanded by about $1/\sin\theta$ (θ refers to the angle between the FIB ion beam and sample),[21] it could calculate the expanded thickness of each layer and differentiate layers.

TEC: The correlation equation of thermal expansion coefficient was defined as follows:[22]

$$\alpha_V = \frac{\Delta V}{V_0 \times \Delta T} \quad (1)$$

where α_V is the volume, TEC, V_0 is the volume at 0 °C, ΔV is the volume difference with temperature and ΔT is the temperature difference.

XRD and Pole Figure: It was obtained by using a PANalytical Xpert Materials Research diffractometer system with a Cu Kα radiation source

(λ = 0.1541 nm) at 45 kV and 40 mA. A receiving slit of 3–8 mm^2 was used to measure the (100) pole figure with background subtraction. The defocused errors and pole figures were corrected and calculated, respectively, using the texture analysis software X'pert Texture from PANalytical B.V version 1.1a

Contact Angle: The hydrophobicity was measured by the sessile drop method using a Rame-Hart Model 250 Goniometer with deionized (DI) water as a reference. DI water droplets (100 µL) were deposited on the substrate and the contact angles between the droplets and the substrate surface were determined.

SCLC: To investigate SCLC measurement, All *J–V* curves for electron-only devices were measured by using a source meter (Keithley 2400) in the dark condition. To calculate the density of traps for control and n-BABr deposited samples, the equation below was used.[23]

$$V_{TFL} = \frac{(e \times N_t \times L^2)}{(2 \times \varepsilon \times \varepsilon_0)} \quad (2)$$

Where V_{TFL} is the trap-filled limit voltage, e is the elementary charge ($\approx 1.6 \times 10^{-19}$ C), N_t is the density of electron traps, L is the thickness of perovskite (≈360 nm), ϵ is the permittivity (25.5) extracted from the literature.[24] The vacuum permittivity, ϵ_0 is 8.85×10^{-12} C V^{-1} m^{-1}.

GIWAXS: It patterns of samples were acquired at the 8-ID-E beamline in the Argon National Laboratory, USA. A Mar345 image plate detector was used to capture the scattering patterns. The sample-to-detector distance is 315.6 mm, which was calibrated from the AgBe standard. The wavelength of the incident X-rays is 1.32 Å. Typical GIWAXS patterns were obtained from an incidence angle of 0.1° to 0.4°.

SSPL and Time-Resolved Photoluminescence (TRPL): For the PL and TRPL spectroscopy, a time-correlated single-photon counting module (TCSPC FluoTime 300 by picoquant, GmbH). The sample excited used LDH-P-C-520 (picoquant 520 nm pulse has 130 ps FWHM) laser source, PDL 820 (picoquant) laser driver, and UV-red-PMT monochrometer (MSH300PQ-0002, picoquant). The PL measured 5 MHz frequency, 131.68 µJ cm^{-2} per pulse energy density. The TRPL measured 3.2 MHz frequency, 87.1 nJ cm^{-2} per pulse energy density.

Density-Functional Theory Calculations: Hybrid density functional calculations were performed to investigate the defect properties of SnO_2. The projector-augmented wave method was used as implemented[25] in the Vienna ab initio Simulation Package.[26] The hybrid density function suggested by Heyd, Scuseria, and Ernzerhof (HSE) was used for the exchange-correlation.[27] The energy cutoff for the plane waves was set to 400 eV, and the atomic structures were optimized until the residual forces were below 0.01 eV $Å^{-1}$. The optimized lattice constants of SnO_2 were 4.757, 4.757, and 3.193 Å, and the bandgap was calculated to be 2.89 eV. For defect calculations, a 3 × 3 × 3 k-point was used for a 2 × 2 × 3 supercell (72-atoms cell) throughout the study. The defect formation energy (E_f) is given as

$$E_f(D) = E_{tot}(D) - E_{tot}(0) - \sum_i n_i \mu_i + qE_F + E_{corr} \quad (3)$$

where $E_{tot}(D)$ and $E_{tot}(0)$ are the total energy of the supercell with and without a defect D, respectively.[28] The variables n_i and μ_i are the number of species i added to the supercell in forming the defect and the corresponding chemical potential, respectively. E_F is the Fermi level and E_{corr} is the correction term to remove spurious interaction between charges. The chemical potential of H, Br, and O was obtained from H_2 molecule, C_{mca} Br, and O_2 molecule.

TCAD: To understand the underlying physical mechanisms in the solar cells, a commercial software package, Senaturus TCAD was used to simulate the device's operation. The exact cell structure was reproduced in the simulator, followed by a meshing process to divide the structure into many small elements to facilitate finite difference calculation. Photogeneration within the cells was computed with the simple optical beam absorption method based on the Beer–Lambert law. The ambient temperature in the simulation is set at 298.15 K to match the standard testing condition. The key semiconductor material parameters for electron simulation are listed in Table S5 (Supporting Information) and obtained either from in-house characterization or from the literature. With these parameters, the thermal equilibrium condition was first computed by solving five semiconductor equations, i.e., the Poisson, drift-diffusion, and carrier continuity equations numerically. Afterward, bias voltage and wavelengths were ramped to mimic light *J–V* and EQE behavior. For effective carrier transport from BA_2PbBr_4 to SnO_2, the electron tunneling mechanism was also found to be necessary.

Supporting Information

Supporting Information is available from the Wiley Online Library or from the author.

Acknowledgements

M.L., J.L., and E.C. contributed equally to this work. J.S.Y. acknowledges support from the Australian Research Council through Discovery Grants and the Royal Society research grant (RGS/R1/221369) and the support by the National Research Foundation of Korea (NRF) grant funded by the Korean government (MEST) (RS-2023-00257494 and 2022H1D3A2A01082324). J. S. acknowledges support from the ARC Centre of Excellence in Future Low Energy Electronics Technologies (FLEET). The authors acknowledge the scientific and technical assistance of the Electron Microscope Unit and Solid State & Elemental Analysis Unit at the University of New South Wales (UNSW). D. H. S acknowledges the support of the Korea Institute of Energy Technology Evaluation and Planning (KETEP) and the Ministry of Trade, Industry & Energy (MOTIE) of the Republic of Korea (No. 20224000000100). J. H. N. acknowledges the support of the National Research Foundation of Korea (NRF) grant funded by the Korea government (MSIP) (grant nos. RS-2023-00208467) and the Korea Institute of Energy Technology Evaluation and Planning (KETEP) from the Ministry of Trade, Industry, and Energy (grant nos. 20214000000680). This research used resources of the Advanced Photon Source; a US Department of Energy (DOE) Office of Science user facility operated for the DOE Office of Science by Argonne National Laboratory under Contract No. DE-AC02-06CH11357.

Open access publishing facilitated by University of New South Wales, as part of the Wiley - University of New South Wales agreement via the Council of Australian University Librarians.

Conflict of Interest

The authors declare no conflict of interest.

Data Availability Statement

The data that support the findings of this study are available on request from the corresponding author. The data are not publicly available due to privacy or ethical restrictions.

Keywords

2D perovskite, indoor perovskite solar cells, tunneling effect, wide bandgap

Received: February 7, 2024
Revised: July 21, 2024
Published online: August 15, 2024

[1] a) L. Liu, X. Guo, C. Lee, *Nano Energy* **2021**, *88*, 106304; b) M. Majid, S. Habib, A. R. Javed, M. Rizwan, G. Srivastava, T. R. Gadekallu, J. C.-W. Lin, *Sensors* **2022**, *22*, 2087; c) S. Li, L. D. Xu, S. Zhao, *Inform. Systems Front.* **2015**, *17*, 243.
[2] A. Mérida García, J. Gallagher, A. McNabola, E. Camacho Poyato, P. Montesinos Barrios, J. A. Rodríguez Díaz, *Renew. Energy* **2019**, *140*, 895.
[3] L. K. Jagadamma, S. Wang, *Front. Chem.* **2021**, *9*, 632021.
[4] C. Polyzoidis, K. Rogdakis, E. Kymakis, *Adv. Energy Mater.* **2021**, *11*, 2101854.
[5] K.-L. Wang, Y.-H. Zhou, Y.-H. Lou, Z.-K. Wang, *Chem. Sci.* **2021**, *12*, 11936.
[6] S. Tao, I. Schmidt, G. Brocks, J. Jiang, I. Tranca, K. Meerholz, S. Olthof, *Nat. Commun.* **2019**, *10*, 2560.
[7] D. Guo, V. M. Caselli, E. M. Hutter, T. J. Savenije, *ACS Energy Lett.* **2019**, *4*, 855.
[8] Q. Wang, Q. Dong, T. Li, A. Gruverman, J. Huang, *Adv. Mater.* **2016**, *28*, 6734.
[9] U. Würfel, A. Cuevas, P. Würfel, *IEEE J. Photovoltaics* **2015**, *5*, 461.
[10] J. C. Blancon, A. V. Stier, H. Tsai, W. Nie, C. C. Stoumpos, B. Traoré, L. Pedesseau, M. Kepenekian, F. Katsutani, G. T. Noe, J. Kono, S. Tretiak, S. A. Crooker, C. Katan, M. G. Kanatzidis, J. J. Crochet, J. Even, A. D. Mohite, *Nat. Commun.* **2018**, *9*, 2254.
[11] C. Deng, J. Wu, Y. Yang, Y. Du, R. Li, Q. Chen, Y. Xu, W. Sun, Z. Lan, P. Gao, *ACS Energy Lett.* **2023**, *8*, 666.
[12] H. Zhu, Q. Li, C. Yang, Q. Zhang, Y. Ren, Q. Gao, N. Wang, K. Lin, J. Deng, J. Chen, *J. Am. Chem. Soc.* **2018**, *140*, 7403.
[13] a) D.-J. Xue, Y. Hou, S.-C. Liu, M. Wei, B. Chen, Z. Huang, Z. Li, B. Sun, A. H. Proppe, Y. Dong, M. I. Saidaminov, S. O. Kelley, J.-S. Hu, E. H. Sargent, *Nat. Commun.* **2020**, *11*, 1514; b) R. Xu, F. Pan, J. Chen, J. Li, Y. Yang, Y. Sun, X. Zhu, P. Li, X. Cao, J. Xi, J. Xu, F. Yuan, J. Dai, C. Zuo, L. Ding, H. Dong, A. K.-Y. Jen, Z. Wu, *Adv. Mater.* **2024**, *36*, 2308039.
[14] K. A. Parrey, S. G. Ansari, A. Aziz, A. Niazi, *Mater. Chem. Phys.* **2020**, *241*, 122387.
[15] X. Wang, K. Rakstys, K. Jack, H. Jin, J. Lai, H. Li, C. S. K. Ranasinghe, J. Saghaei, G. Zhang, P. L. Burn, I. R. Gentle, P. E. Shaw, *Nat. Commun.* **2021**, *12*, 52.
[16] V. W. Bergmann, S. A. L. Weber, F. J. Ramos, M. K. Nazeeruddin, M. Grätzel, D. Li, A. L. Domanski, I. Lieberwirth, S. Ahmad, R. Berger, *Nat. Commun.* **2014**, *5*, 5001.
[17] T.-H. Lai, S.-W. Tsang, J. R. Manders, S. Chen, F. So, *Mater. Today* **2013**, *16*, 424.
[18] a) R. Wang, M. Li, Z. Ma, Z. He, Y. Dong, Y. Zhang, Z. Xu, G. Su, Z. Tan, *Chem. Commun.* **2023**, *59*, 6255; b) C. Chen, Z. Song, C. Xiao, R. A. Awni, C. Yao, N. Shrestha, C. Li, S. S. Bista, Y. Zhang, L. Chen, R. J. Ellingson, C.-S. Jiang, M. Al-Jassim, G. Fang, Y. Yan, *ACS Energy Lett.* **2020**, *5*, 2560; c) Y. Zhao, C. Wang, T. Ma, L. Zhou, Z. Wu, H. Wang, C. Chen, Z. Yu, W. Sun, A. Wang, H. Huang, B. Zou, D. Zhao, X. Li, *Energy Environ. Sci.* **2023**, *16*, 2080; d) P. Hang, C. Kan, B. Li, Y. Yao, Z. Hu, Y. Zhang, J. Xie, Y. Wang, D. Yang, X. Yu, *Adv. Funct. Mater.* **2023**, *33*, 2214381; e) H. Liu, J. Dong, P. Wang, B. Shi, Y. Zhao, X. Zhang, *Adv. Funct. Mater.* **2023**, *33*, 2303673; f) H. Chen, A. Maxwell, C. Li, S. Teale, B. Chen, T. Zhu, E. Ugur, G. Harrison, L. Grater, J. Wang, Z. Wang, L. Zeng, S. M. Park, L. Chen, P. Serles, R. A. Awni, B. Subedi, X. Zheng, C. Xiao, N. J. Podraza, T. Filleter, C. Liu, Y. Yang, J. M. Luther, S. De Wolf, M. G. Kanatzidis, Y. Yan, E. H. Sargent, *Nature* **2023**, *613*, 676; g) Y. Tang, Y. Zhang, X. Zhou, T. Huang, K. Shen, K. Zhang, X. Du, T. Shi, X. Xiao, N. Li, C. J. Brabec, Y. Mai, F. Guo, *Nano Energy* **2023**, *114*, 108653.
[19] B. Wu, K. Fu, N. Yantara, G. Xing, S. Sun, T. C. Sum, N. Mathews, *Adv. Energy Mater.* **2015**, *5*, 1500829.
[20] T. W. Kim, S. Uchida, *Hitachi Sci. Instrum. News* **2019**, *13*, 1.
[21] a) K. Sardashti, R. Haight, R. Anderson, M. Contreras, B. Fruhberger, A. C. Kummel, *ACS Appl. Mater. Interfaces* **2016**, *8*, 14994; b) P. Cui, D. Wei, J. Ji, H. Huang, E. Jia, S. Dou, T. Wang, W. Wang, M. Li, *Nat. Energy* **2019**, *4*, 150.
[22] J. Chen, L. Hu, J. Deng, X. Xing, *Chem. Soc. Rev.* **2015**, *44*, 3522.
[23] M. H. Ann, J. Kim, M. Kim, G. Alosaimi, D. Kim, N. Y. Ha, J. Seidel, N. Park, J. S. Yun, J. H. Kim, *Nano Energy* **2020**, *68*, 104321.
[24] B. Zhao, G. Niu, Q. Dong, J. Liu, N. Li, J. Li, L. Wang, *J. Mater. Chem. A* **2018**, *6*, 23797.
[25] P. E. Blöchl, *Phys. Rev. B* **1994**, *50*, 17953.
[26] G. Kresse, J. Furthmüller, *Phys. Rev. B* **1996**, *54*, 11169.
[27] J. Heyd, G. E. Scuseria, M. Ernzerhof, *J. Chem. Phys.* **2003**, *118*, 8207.
[28] S. Kim, S. N. Hood, J.-S. Park, L. D. Whalley, A. Walsh, *J. Phys. Energy* **2020**, *2*, 036001.